throughout this study is only 27 Hz, but this can be attributed to our use of an iron-cored electromagnet to apply the rotating field. If these devices were mounted on a high-frequency stripline, operating speed would ultimately be limited by the domain wall propagation time through a single gate. For domain wall mobility, $\mu = 30\ ms^{-1}\ Oe^{-1}$ (*23*), and current experimental conditions, we calculate an operating frequency of >200 MHz for devices with a 1-μm radius of curvature. This operating frequency will increase as the size of the gate is further reduced. We estimate the switching energy of the magnetic NOT gates presented here to be 35 eV per transition (*24*) ($1400kT$, where $k$ is Boltzmann's constant and $T$ is room temperature), indicating very great stability of data against thermal loss.

A particularly interesting feature of these NOT gates is that they can perform real logic operations on real data without the use of any semiconductor material. This makes scaling to the nanoscale very simple: first, because of the much higher carrier density in metals than in semiconductors; and second, because of the lack of multilayer heterostructures requiring precise alignment. Domain wall widths should not limit this miniaturization because we expect their value to decrease with track widths, tending to the exchange length (5 nm for Permalloy) as track widths approach the film thickness. However, it is currently unclear whether miniaturization will cause appreciable domain wall pinning at defects.

Three further logic elements are required in addition to the NOT gate and shift register described here in order to make a fully universal logic architecture. These are a two-input logic gate that performs an AND, OR, or XOR function; a fan-out structure that converts one domain wall into two walls; and a structure that allows magnetic tracks to cross over each other. An advantage of the rotating clock field is that domain walls move in orthogonal directions at different times. Consequently, it may be possible to cross two tracks in the same plane without interference of the magnetic signals. Domain wall replication should be possible by simply splitting a magnetic track into two branches. The extra energy needed to create the second domain wall comes from the work done by the applied magnetic field against the domain wall pinning force at the junction. The opposite structure, in which two tracks feed into one, may by used to achieve the two-input logic function, using the wire-OR method from microelectronics. In this case, some magnetic biasing will also be required, analogous to the pull-up resistor in the wire-OR scheme.

For a fully functioning nanomagnetic logic system, it will also be necessary to interface conventional electronic signals. Data can be written into the magnetic structures by a current-carrying stripline; and data can be read out by incorporating spin tunnel junctions or spin valves into magnetic tracks or, alternatively, by measuring domain wall resistance.

### References and Notes


1. G. A. Prinz, *Science* **282**, 1660 (1998).
2. S. A. Wolf *et al.*, *Science* **294**, 1488 (2001).
3. D. Loss, D. P. DiVicenzo, *Phys. Rev. A* **57**, 120 (1998).
4. S. Koshihara *et al.*, *Phys. Rev. Lett.* **78**, 4617 (1997).
5. H. Ohno *et al.*, *Nature* **408**, 944 (2000).
6. D. J. Monsma, R. Vlutters, J. C. Lodder, *Science* **281**, 407 (1998).
7. R. Fiederling *et al.*, *Nature* **402**, 787 (1999).
8. Y. Ohno *et al.*, *Nature* **402**, 790 (1999).
9. R. K. Kawakami *et al.*, *Science* **294**, 131 (2001).
10. J. H. Smet *et al.*, *Nature* **415**, 281 (2002).
11. M. N. Baibich *et al.*, *Phys. Rev. Lett.* **61**, 2472 (1988).
12. J. S. Moodera, L. R. Kinder, T. M. Wong, R. Meservey, *Phys. Rev. Lett.* **74**, 3273 (1995).
13. R. P. Cowburn, M. E. Welland, *Science* **287**, 1466 (2000).
14. http://math.nist.gov/oommf/
15. T. Ono *et al.*, *Science* **284**, 468 (1999).
16. G. Xiong, D. A. Allwood, M. D. Cooke, R. P. Cowburn, *Appl. Phys. Lett.* **79**, 3461 (2001).
17. R. P. Cowburn, D. K. Koltsov, A. O. Adeyeye, M. E. Welland, *Appl. Phys. Lett.* **73**, 3947 (1998).
18. The magnetization transitions shown in Fig. 2C indicate that domain walls require a parallel magnetic field of just 3 Oe to propagate in continuous wire sections, which is when the orthogonal component of the rotating field is close to its maximum value.
19. W. C. Black Jr., B. Das, *J. Appl. Phys.* **87**, 6674 (2000).
20. C.-Y. You, S. D. Bader, *J. Appl. Phys.* **87**, 5215 (2000).
21. In the previous case of one NOT gate in a feedback loop, no pulsed-field initialization was required owing to the simpler topology involved.
22. W. A. Triebel, A. E. Chu, *Handbook of Semiconductor and Bubble Memories* (Prentice-Hall, Englewood Cliffs, NJ, 1982).
23. M. Redjdal, J. Guisti, M. F. Ruane, F. B. Humphrey, *J. Appl. Phys.*, **91**, 7547 (2002).
24. Switching energy was calculated with the area of the magnetization hysteresis loop and suitable bulk constants.


25. This work was supported by Eastgate Investments Ltd.

6 February 2002; accepted 19 April 2002


# Ferroelectric $Bi_{3.25}La_{0.75}Ti_3O_{12}$ Films of Uniform *a*-Axis Orientation on Silicon Substrates


**Ho Nyung Lee, Dietrich Hesse, Nikolai Zakharov, Ulrich Gösele**



**The use of bismuth-layered perovskite films for planar-type nonvolatile ferroelectric random-access memories requires films with spontaneous polarization normal to the plane of growth. Epitaxially twinned *a* axis–oriented La-substituted $Bi_4Ti_3O_{12}$ (BLT) thin films whose spontaneous polarization is entirely along the film normal were grown by pulsed laser deposition on yttria-stabilized zirconia-buffered Si(100) substrates using $SrRuO_3$ as bottom electrodes. Even though the (118) orientation competes with the (100) orientation, epitaxial films with almost pure (100) orientation were grown using very thin, strained $SrRuO_3$ electrode layers and kinetic growth conditions, including high growth rates and high oxygen background pressures to facilitate oxygen incorporation into the growing film. Films with the *a*-axis orientation and having their polarization entirely along the direction normal to the film plane can achieve a remanent polarization of 32 microcoulombs per square centimeter.**


Ferroelectric bismuth-layered perovskite films are being studied for use as nonvolatile digital memories. Polycrystalline films, such as $SrBi_2Ta_2O_9$ (SBT) (*1*) and La-substituted $Bi_4Ti_3O_{12}$, including $Bi_{3.25}La_{0.75}Ti_3O_{12}$ (BLT) (*2*), are of great interest in part because of their high fatigue endurance. However, randomly oriented polycrystalline films have certain limitations, and they may have unacceptable cell-to-cell variations when the lateral size of the ferroelectric cells is below 100 nm, as is required for gigabit memories (*3*).

Conceptually, epitaxially grown films should overcome this nonuniformity problem, and numerous attempts have been made to grow thin films by pulsed laser deposition (PLD) (*4*–*8*) as well as other methods (*9*–*12*). Because of their highly anisotropic structure [$Bi_4Ti_3O_{12}$ is pseudo-orthorhombic with $a = 0.545$ nm, $b = 0.541$ nm, and $c = 3.283$ nm (*13*)], epitaxial thin films of these materials can easily be grown with the [001] axis perpendicular to the film plane (i.e., in the so-called *c*-axis orientation). However, *c* axis–oriented films have a negligible polarization component along the film normal, because the vector of the (major) spontaneous polarization in these layered perovskite materials is along the *a* axis (*13*, *14*). Recent efforts have concentrated on the growth of epitaxial films with non–*c*-axis orientations


Max-Planck-Institut für Mikrostrukturphysik, Weinberg 2, D-06120 Halle/Saale, Germany.

(*5–8, 11, 15–17*), including (118) and (104) for BLT and (116) and (103) for SBT. These orientations have the spontaneous polarization vector inclined to the film plane. The best choice would, however, be (100)-oriented or *a* axis–oriented films, because in this case the (major) polarization vector is perpendicular to the film plane, resulting in a maximum value of the remanent polarization (*18*). Such films have not yet been grown on electroded silicon substrates, as is desired for memories, but rather on special complex-oxide single-crystal substrates without bottom electrodes (*9, 12*), which are not suitable for microelectronic applications.

By covering Si(100) substrates with very thin, strained (110)-oriented $SrRuO_3$ electrode layers on (100)-oriented yttria-stabilized zirconia (YSZ) buffer layers, *a* axis–oriented BLT films have been produced successfully. BLT films have been grown in the (118) orientation on nonstrained, thick (50 nm) bottom $SrRuO_3$ electrodes (*17*). Replacement of nonstrained electrodes by epitaxially strained electrodes is the first important step in growing (100)-oriented BLT films. However, for standard deposition conditions, the (100) orientation still competes with the (118) orientation, and only through specific deposition conditions can the volume percentage of (118)-oriented grains be suppressed to less than 1%.

The BLT films and the $SrRuO_3$ and YSZ layers were grown in situ by PLD on Si(100) substrates with the use of a KrF excimer laser ($\lambda$ = 248 nm). Details of the deposition conditions were reported in (*6, 17*). For BLT deposition, a bismuth-excess $Bi_{3.75}La_{0.75}Ti_3O_{12}$ target was used. The $SrRuO_3$ thickness ($t$ = 10 to 50 nm), substrate temperature ($T$ = 650° to 825°C), laser fluence ($J$ = 1.7 to 4.0 J/cm$^2$), laser repetition rate ($f$ = 2 to 10 Hz), and oxygen pressure ($P$ = 30 to 100 Pa) were systematically varied; the YSZ thickness (60 nm) and the number of laser pulses (3000) were fixed. All the varied parameters turned out to play an important role in determining the orientation and quality of the BLT films. The volume fractions of the (100) and (118) orientations were evaluated by comparing the corresponding x-ray diffraction (XRD) intensities in $\phi$ scans. The latter were recorded using the BLT 111 reflection giving peaks at $\psi$ = 46° and 36°, corresponding to (100) and (118) orientations, respectively. ($\psi$ = 90° corresponds to the substrate surface being parallel to the plane defined by the incident and reflected x-ray beams.)

In addition to determining the volume fraction $\alpha_{(100)}$ of the (100)-oriented part of the BLT film by XRD scans, $\alpha_{(100)}$ could also be roughly estimated from the morphology of the grains visible in atomic force microscopy (AFM) images. Two distinct shapes of grains are observed, namely long needle-like ones and more or less equiaxed ones (Fig. 1). The long grains correspond to the (118)-oriented part of the film, whereas the equiaxed grains represent the (100)-oriented part (*7, 8, 16*). The needle-like (118)-oriented BLT grains occur with four different azimuthal orientations, corresponding to the four possible azimuthal orientations of the $SrRuO_3$ grains in (110)-oriented $SrRuO_3$ layers on (100)-oriented YSZ buffer layers (Fig. 1D) (*15, 16, 19*). As a consequence, azimuthal difference angles of 19.5° occur between the needle-like (118)-oriented BLT grains growing on top of the $SrRuO_3$ grains.

The optimum substrate temperature for the (100)-oriented growth of BLT was found by depositing BLT films at different temperatures onto YSZ(100) single-crystal substrates covered with (110)-oriented $SrRuO_3$ layers and determining the volume fraction $\alpha_{(100)}$. $\alpha_{(100)}$ was as low as 4% at $T$ = 650°C (Fig. 1A) and reached its maximum of 46% at $T$ = 765°C (*20*) under the same deposition conditions of $J$ = 2.3 J/cm$^2$, $f$ = 5 Hz, and $P$ = 40 Pa. A further increase of $\alpha_{(100)}$ was possible by reducing the thickness of the (110)-oriented $SrRuO_3$ electrode layer down to 10 nm, which resulted in an additional increase of $\alpha_{(100)}$ from 46% to 78%. This drastic effect is most probably due to the thin $SrRuO_3$ layer being strained as a result of the influence of the lattice mismatch (−6.3%) between $SrRuO_3$ ($a$ = 3.93 nm) and YSZ ($a$ = 5.14 nm) along the direction $SrRuO_3$ [$\bar{1}$11] ∥ YSZ[011]. This strain results in an increased $SrRuO_3$ lattice parameter, which reduces the BLT-$SrRuO_3$ lattice misfit of nominally +4.6% along the direction BLT[001] ∥ $SrRuO_3$[001], thus providing better nucleation conditions for (100)-oriented BLT grains relative to (118)-oriented grains. The same effect was observed for BLT films grown on the YSZ-buffered Si(100) substrates. A further increase of $\alpha_{(100)}$ was achieved by a systematic variation of the other deposition conditions. Finally, a value of $\alpha_{(100)}$ = 99% was attained at $T$ = 765°C, $J$ = 3.4 J/cm$^2$, $f$ = 7 Hz, and $P$ = 100 Pa (Fig. 1C). Deviations from these conditions resulted in intermediate values of $\alpha_{(100)}$, as shown in Fig. 1B, where optimum conditions were used but for $J$ = 1.7 J/cm$^2$ and $P$ = 40 Pa, resulting in $\alpha_{(100)}$ = 48%.

The high oxygen pressure necessary to grow *a* axis–oriented BLT films can most likely be explained in terms of effects related to an improved oxygen incorporation into the growing film as a result of increased collisions between vapor and ambient oxygen gas (*21, 22*). If an enhanced oxidation of bismuth is one such effect, the bismuth desorption from the *a* axis–oriented BLT films may be reduced as a result. The *a* axis–oriented BLT films have the $Bi_2O_2$ layers perpendicular to the film plane, so that the desorption of bismuth could be rather easy at the relatively high substrate temperature used. In addition, the high laser repetition rate will favor suppression of desorption events by a more frequent supply of ablated species. Moreover, the high film growth rate resulting from the high laser repetition rate probably favors the (100) orientation by a kinetic growth mechanism, as is the case for (110)-oriented $TiS_2$ films (*23*) and (100)-oriented $YBa_2Cu_3O_{7-\delta}$ films (*24–26*), both of which involve a layered crystal struc-

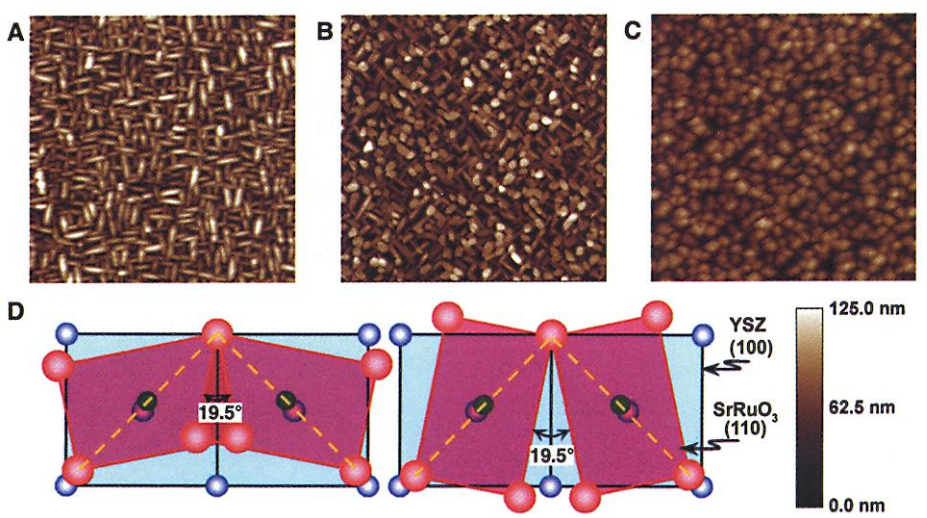


**Fig. 1.** (**A** to **C**) AFM topography images (5 μm by 5 μm) of BLT films grown under different conditions: (A) on $SrRuO_3$(110)-YSZ(100) at $T$ = 650°C, $t$ = 50 nm, $J$ = 2.3 J/cm$^2$, $f$ = 5 Hz, and $P$ = 40 Pa; (B) on $SrRuO_3$(110)-YSZ(100)-Si(100) at $T$ = 765°C, $t$ = 10 nm, $J$ = 1.7 J/cm$^2$, $f$ = 5 Hz, and $P$ = 40 Pa; and (C) on $SrRuO_3$(110)-YSZ(100)-Si(100) at $T$ = 765°C, $t$ = 10 nm, $J$ = 3.4 J/cm$^2$, $f$ = 7 Hz, and $P$ = 100 Pa. In (C), the height scale ranges from 0 to 200 nm; the height scale for (A) and (B) is shown at the lower right. (**D**) Schematic of the diagonal-type rectangle-on-cube epitaxy of $SrRuO_3$(110) on YSZ(100) with four variants of $SrRuO_3$ on YSZ, showing the origin of the ~20° azimuthal rotation.

ture. Indeed, (100)-oriented films showed a considerably larger film thickness than an almost (118)-oriented film for the same number of laser pulses. This effect is probably due to a higher growth rate along the *a* axis and/or a reduction of desorption.

The crystallographic orientation, epitaxial relationship, and microstructure of *a* axis–oriented BLT films with different values of $\alpha_{(100)}$ were analyzed by XRD scans and transmission electron microscopy (TEM) in plan view and cross section. An XRD θ-2θ scan (Fig. 2A) and a pole figure of the BLT 117 reflection (Fig. 2B) were recorded from the sample shown in Fig. 1C ($\alpha_{(100)}$ = 99%). The BLT 200/020 and the YSZ 200 and 400 peaks are clearly seen. $SrRuO_3$ peaks are not visible because the layer thickness is very low (10 nm). The full width at half-maximum (FWHM) of the 200/020 peak in an ω scan was 0.83°, demonstrating the good crystallinity. Detailed XRD investigations showed that the BLT film has lattice constants $a$ = 0.542 nm, $b$ = 0.541 nm, and $c$ = 3.271 nm. Several pole figures and φ scans were recorded. Figure 2B is a pole figure using the 117 reflection of the BLT film shown in Figs. 2A and 1C. There are four sets of peaks at $\psi \approx 57°$, confirming the (100) orientation of the film, because the angle between the (100) plane and the diffracting (117) plane is 56.9°. Each set of peaks, however, consists of two subsets (of two peaks each) with an offset $\Delta\phi \approx 20°$ as marked in Fig. 2B, showing that four different azimuthal domains are occurring within the same *a* axis–oriented BLT film as a result of the four azimuthal domains within the underlying $SrRuO_3$ electrode layer (Fig. 1D). This mix of four azimuthal domains (or twins) obviously gives rise to the grainy structure of the films (compare to Fig. 1C)—a fact that otherwise would be difficult to understand in a uniformly (100)-oriented film. The corresponding epitaxy relationship is BLT(100) ∥ $SrRuO_3$(110) ∥ YSZ(100) ∥ Si(100); BLT[001] ∥ $SrRuO_3$[001], where $SrRuO_3[\bar{1}11]$ ∥ YSZ⟨011⟩ ∥ Si⟨011⟩ including four azimuthal domains (*15, 16*).

TEM investigations confirmed the *a*-axis orientation, as shown in Fig. 3. Both plan-view and cross-sectional TEM images of a BLT film with $\alpha_{(100)}$ = 90% clearly show the (002) lattice fringes. As plan-view TEM images (Fig. 3, A and B) show, the *c* axis of the *a* axis–oriented grains indeed lies in the film plane. As a result of the four azimuthal orientations discussed above, the electron diffraction pattern (Fig. 3A, inset) consists of four rows of BLT (00*l*) reflections that include azimuthal difference angles of ~20° when considered pairwise. Cross-section TEM images of the entire BLT-$SrRuO_3$-YSZ-Si heterostructure (Fig. 3C) and high-resolution TEM investigations of cross-section samples (Fig. 3D) confirm the (100) orientation of the film. In the (100)-oriented BLT grain marked "M" in Fig. 3C, the (002) BLT fringes extending vertically (at an angle of 90° with respect to the film plane) can clearly be recognized. The inset shows the corresponding diffraction pattern. The small grain marked "N" is a (118)-oriented grain in which, upon close inspection, the (002) fringes can be seen at an angle of about 45° with respect to the film plane. In the rest of the visualized film area in Fig. 3C, no fringes can be seen, because the

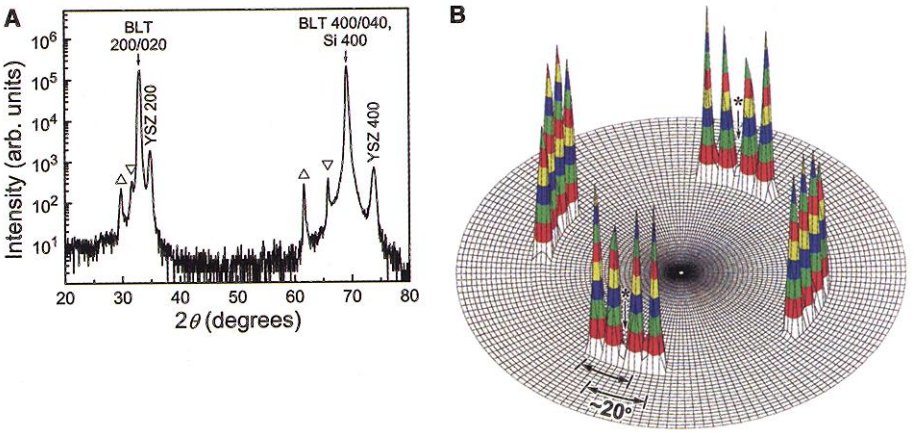


**Fig. 2.** X-ray diffraction (**A**) θ-2θ scan and (**B**) pole figure (using the BLT 117 peak) of an almost purely *a* axis–oriented BLT film ($\alpha_{(100)}$ = 99%). The peaks due to the remaining Cu-K$\beta_1$ and the W-L$\alpha_1$ radiation are labeled Δ and ∇, respectively, in (A). The latter results from the tungsten contamination of the x-ray target by the tungsten cathode filament. The peaks labeled with asterisks in (B) originate from a shoulder of the YSZ 111 peak.

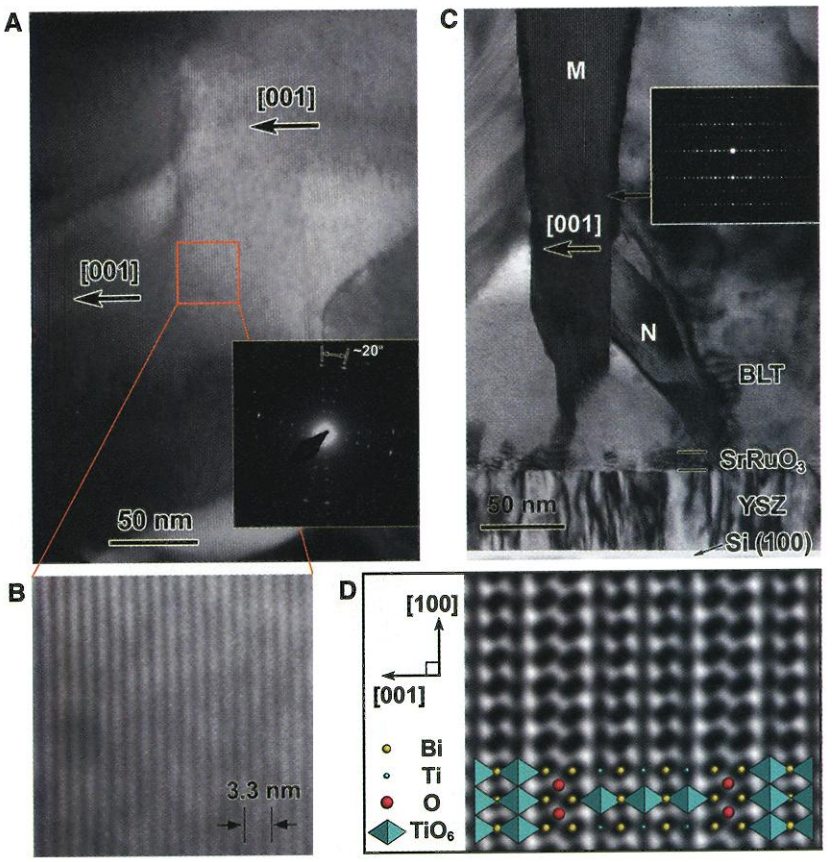


**Fig. 3.** Plan-view (**A** and **B**) and cross-sectional transmission (**C** and **D**) electron micrographs of an *a* axis–oriented film still containing some (118)-oriented grains ($\alpha_{(100)}$ = 90%). The insets are electron diffraction patterns of (100)-oriented areas and show that the *c* axis is lying in the film plane.

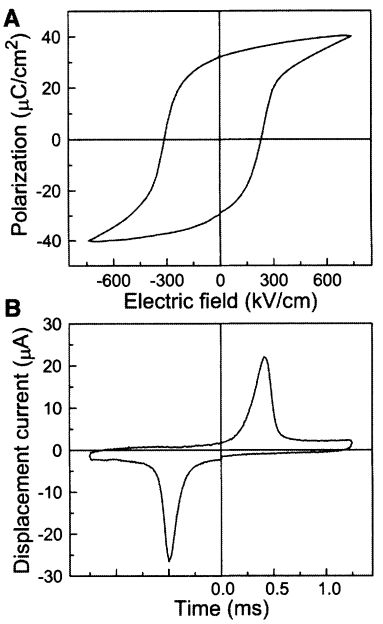


**Fig. 4.** (**A**) *P-E* hysteresis loop of a Pt-BLT(100)-$SrRuO_3$(110) capacitor ($\alpha_{(100)}$ = 99%). (**B**) Displacement current curve recorded during the *P-E* curve measurement. BLT film thickness is 1 μm.

other domains (twins) have different azimuthal orientations. Figure 3D shows a high-resolution structure image of a thin area of grain "M," showing a good correspondence to the inserted structure model.

Ferroelectric polarization–electric field (*P-E*) hysteresis loops and simultaneously recorded displacement currents of BLT films (thickness 1 μm) with $\alpha_{(100)}$ = 99% were recorded at 200 Hz, as shown in Fig. 4. Platinum top electrodes (diameter 100 μm) were sputter-deposited. The films revealed well-saturated hysteresis loops (Fig. 4A) with a remanent polarization and a coercive field of 32 μC/cm² and 265 kV/cm, respectively, for a maximum applied electric field of 740 kV/cm (*18*). The corresponding displacement current curve is shown in Fig. 4B. The polarization corresponds well to the value of 35 μC/cm² that can be calculated using the relation between the major polarization values of BLT and $Bi_4Ti_3O_{12}$ given by Shimakawa *et al.* (*27*) and the polarization value of $Bi_4Ti_3O_{12}$ single crystals given by Cummins and Cross (*14*).

One of the proposed mechanisms for the absence of fatigue in bismuth-layered perovskite films is related to a space-charge compensation near the electrodes by the bismuth oxide double layers (*1*). However, the space-charge compensation is likely to be difficult in films having their $Bi_2O_2$ planes perpendicular to the film plane. Initial fatigue characterization up to $10^9$ cycles (fig. S1) (*28*) shows hardly any fatigue. For actual applications in memory devices, the absence of fatigue in the range of $10^9$ to $10^{12}$ switching cycles will be essential.


**References and Notes**

1. C. A. P. de Araujo, J. D. Cuchiaro, L. D. McMillan, M. C. Scott, J. F. Scott, *Nature* **374**, 627 (1995).
2. B. H. Park *et al.*, *Nature* **401**, 682 (1999).
3. A. Gruverman, *Appl. Phys. Lett.* **75**, 1452 (1999).
4. R. Ramesh *et al.*, *Science* **252**, 944 (1991).
5. J. Lettieri *et al.*, *Appl. Phys. Lett.* **76**, 2937 (2000).
6. H. N. Lee *et al.*, *J. Appl. Phys.* **88**, 6658 (2000).
7. H. N. Lee, D. N. Zakharov, S. Senz, A. Pignolet, D. Hesse, *Appl. Phys. Lett.* **79**, 2961 (2001).
8. H. N. Lee, D. N. Zakharov, P. Reiche, R. Uecker, D. Hesse, *Mater. Res. Symp. Proc.* **688**, C8.5 (2002).
9. S. Y. Wu, W. J. Takei, M. H. Francombe, S. E. Cummins, *Ferroelectrics* **3**, 217 (1972).
10. C. D. Theis *et al.*, *Appl. Phys. Lett.* **72**, 2817 (1998).
11. K. Ishikawa, H. Funakubo, *Appl. Phys. Lett.* **75**, 1970 (1999).
12. S. E. Moon *et al.*, *Appl. Phys. Lett.* **75**, 2827 (1999).
13. A. D. Rae, J. G. Thompson, R. L. Withers, A. C. Willis, *Acta Crystallogr.* **B46**, 474 (1990).
14. S. E. Cummins, L. E. Cross, *J. Appl. Phys.* **39**, 2268 (1968).
15. H. N. Lee *et al.*, *Appl. Phys. A* **71**, 101 (2000).
16. H. N. Lee *et al.*, *Appl. Phys. Lett.* **77**, 3260 (2000).
17. H. N. Lee, D. Hesse, *Appl. Phys. Lett.* **80**, 1040 (2002).
18. In this paper, *a-b* growth twins are not explicitly considered. The difference between the lattice parameters *a* and *b* of BLT is so small that it is difficult to discriminate between them. However, the high value of the remanent polarization of our films implies that there are almost no *a-b* twins present or that the latter are totally switched into the *a*-axis orientation.
19. S. Y. Hou, J. Kwo, R. K. Watts, J. Y. Cheng, D. K. Fork, *Appl. Phys. Lett.* **67**, 1387 (1995).
20. Although this high growth temperature most probably does not comply with memory device fabrication, it can probably be reduced by using other oxidants instead of $O_2$, including nitrous oxide ($N_2O$) or nitrogen dioxide ($NO_2$) (*29, 30*).
21. C. Girault, D. Damiani, J. Aubreton, A. Catherinot, *Appl. Phys. Lett.* **55**, 182 (1989).
22. D. B. Geohegan, *Appl. Phys. Lett.* **60**, 2732 (1992).
23. K. Kanehori, F. Kirino, Y. Ito, K. Miyauchi, T. Kudo, *J. Electrochem. Soc.* **136**, 1265 (1989).
24. J. Fujita, T. Yoshitake, A. Kamijo, T. Satoh, H. Igarashi, *J. Appl. Phys.* **64**, 1292 (1988).
25. C. B. Eom, A. F. Marshall, S. S. Laderman, R. D. Jacowitz, T. H. Geballe, *Science* **249**, 1549 (1990).
26. Q. Zhong, P. C. Chou, Q. L. Li, G. S. Taraldsen, A. Ignatiev, *Physica C* **246**, 288 (1995).
27. Y. Shimakawa *et al.*, *Appl. Phys. Lett.* **79**, 2791 (2001).
28. Materials and methods are available as supplementary material on *Science* Online.
29. G. Koren, A. Gupta, R. J. Baseman, *Appl. Phys. Lett.* **54**, 1920 (1989).
30. M. Kanai, K. Horiuchi, T. Kawai, S. Kawai, *Appl. Phys. Lett.* **57**, 2716 (1990).


31. Supported in part by European Union project IST-2000-28495 (INVEST) (H.N.L.) and by the Deutsche Forschungsgemeinschaft via the Group of Researches FOR 404 at Martin Luther University Halle-Wittenberg.


**Supporting Online Material**

www.sciencemag.org/cgi/content/full/296/5575/2006/DC1
Materials and Methods
Fig. S1

17 January 2002; accepted 10 May 2002

# Design and Control of Wave Propagation Patterns in Excitable Media

**Tatsunari Sakurai, Eugene Mihaliuk, Florin Chirila, Kenneth Showalter***

**Intricate patterns of wave propagation are exhibited in a chemical reaction-diffusion system with spatiotemporal feedback. Wave behavior is controlled by feedback-regulated excitability gradients that guide propagation in specified directions. Waves interacting with boundaries and with other waves are observed when interaction terms are incorporated into the control algorithm. Spatiotemporal feedback offers wide flexibility for designing and controlling wave behavior in excitable media.**

It is now possible to implement control strategies that yield new modes of spatiotemporal behavior in excitable chemical and biological media. Feedback methods have been used to control spatiotemporal activity in the Pt-catalyzed oxidation of CO (*1*), suggesting a means for enhancing catalytic efficiencies, and focused laser light has been used to direct wave propagation in this system by thermally altering local catalytic activity (*2*). Pattern formation (*3–5*) and spiral waves (*6*, *7*) in the Belousov-Zhabotinsky (BZ) reaction (*8*) have also been controlled by using feedback techniques, which points to the possibility of regulating spatiotemporal dynamics in excitable biological tissues. A recent advance in this direction is the control of seizure-like events in hippocampal brain slices with adaptive electric fields (*9*). The ability to manipulate spatiotemporal behavior provides both a means of generating desired dynamical patterns and the tools for probing underlying mechanisms.

Here, we describe the implementation of control methods that yield particle-like waves that propagate in, effectively, user-defined patterns. Unstable waves in the photosensitive BZ reaction (*10*) are stabilized by global feedback that affects the overall excitability of the medium (*11*), and the motion of these

Department of Chemistry, West Virginia University, Morgantown, WV 26506, USA.

*To whom correspondence should be addressed. E-mail: kshowalt@wvu.edu